International Journal of Nanomedicine

Dovepress
Taylor & Francis Group

Open Access Full Text Article

ORIGINAL RESEARCH

ROS-Responsive Nanosystem Targeted Co-Delivery YC-1 and Regorafenib to Alleviate Hypoxia Enhancing Hepatocellular Carcinoma Therapy

Liming Song[1–3], Yahui Wu[1–3], Senfeng Zhao[1–3], Yin Liu[1–3], Zhipu Liu[1–3], Yunpeng Zhai[1–3], Jiahui Cao[1–3], Yaning Xia[4], Ruopeng Liang[1–3], Weijie Wang[1–3], Rongtao Zhu[1–3], Binghua Sun[5], Yupeng Shi[4], Yuling Sun[1–3]

[1]Department of Hepatobiliary and Pancreatic Surgery, The First Affiliated Hospital of Zhengzhou University, Zhengzhou, 450052, People's Republic of China; [2]Institute of Hepatobiliary and Pancreatic Diseases, Zhengzhou University, Zhengzhou, 450052, People's Republic of China; [3]Zhengzhou Basic and Clinical Key Laboratory of Hepatopancreatobiliary Diseases, Zhengzhou, 450052, People's Republic of China; [4]Department of Magnetic Resonance Imaging, The First Affiliated Hospital of Zhengzhou University, Zhengzhou, 450052, People's Republic of China; [5]Department of Gastroenterology, The First Affiliated Hospital of Zhengzhou University, Zhengzhou, 450052, People's Republic of China

Correspondence: Yuling Sun, Department of Hepatobiliary and Pancreatic Surgery, The First Affiliated Hospital of Zhengzhou University, Zhengzhou, 450052, People's Republic of China, Email ylsun@zzu.edu.cn; Yupeng Shi, Department of Magnetic Resonance Imaging, The First Affiliated Hospital of Zhengzhou University, Zhengzhou, 450052, People's Republic of China, Email shiyup@zzu.edu.cn

Purpose: The current treatment of hepatocellular carcinoma (HCC) is confronted with anoxic drug resistance and significant side effects. To address these issues, a Reactive Oxygen Species (ROS)-responsive and targeted nano drug delivery system named REG/YC-1@PTP-RGD NPs (RYP-RGD NPs) was designed for the co-delivery of Regorafenib (REG) and the hypoxia inhibitor 3-(5′-hydroxymethyl-2′-furyl)-1-benzylindazole (YC-1).

Methods: RYP-RGD NPs were fabricated through the self-assembly method. A series of techniques, such as transmission electron microscopy (TEM), UV-visible spectroscopy, and others, were employed to characterize their properties. In Vitro investigations encompassed drug release assays, cytotoxicity evaluations using Cell Counting Kit-8 (CCK-8) and other methods, cell uptake experiments, and Western blot analysis. In vivo, the biodistribution of RYP-RGD NPs was tracked by IVIS imaging, and their antitumor efficacy and biosafety were assessed in a HepG2 tumor-bearing mouse model with histological staining and biochemical analysis.

Results: RYP-RGD NPs exhibited a spherical morphology with an appropriate size and excellent dispersion. They demonstrated ROS-triggered drug release behavior. In vitro studies revealed good tumor-targeting ability, enhanced cytotoxicity against HCC cells, and the downregulation of hypoxia-inducible factor-1α (HIF-1α) by YC-1. In vivo experiments showed improved tumor targeting, significant inhibition of tumor growth, and lower toxicity compared to single drugs.

Conclusion: The successfully developed RYP-RGD NPs offer a novel strategy for HCC treatment. They enhance drug targeting, synergistically boost the therapeutic effect, and maintain biosafety, showing great potential for clinical translation.

Keywords: drug delivery, reactive oxygen species, hypoxia, regorafenib, nanocarrier

Introduction

Hepatocellular carcinoma (HCC) is the sixth most lethal cancer in the world, with an average of 800,000 new cases diagnosed each year.[1,2] However, in the face of such a huge patient population, the current treatment options for liver cancer are not abundant. Early HCC can be effectively treated by surgical resection and interventional therapy.[3–5] However, the reality is that most HCC patients are diagnosed at an advanced stage and therefore miss the best opportunity to access surgery. Chemotherapy is an important treatment for patients with advanced liver cancer, which can directly kill cancer cells, slow down tumor growth, and give them the opportunity to operate again.[6]

Received: 3 February 2025
Accepted: 18 June 2025
Published: 1 July 2025

As an oral multikinase (MKI) inhibitor of vascular endothelial growth factor receptor, sorafenib became the first first-line drug approved by FDA for the treatment of HCC due to its powerful anti-tumor and anti-angiogenic effects.[7,8] However, due to the heterogeneity and evolutionary nature of tumors, many patients who are resistant to sorafenib have appeared clinically. Regorafenib is another oral multikinase inhibitor that acts on VEGFR1-3, PDGFRB, and mutant cancer-causing kinases KIT, RET, and B-RAF.[9,10] In 2017, it was approved by the FDA for the treatment of patients with advanced HCC who had previously been treated with sorafenib.[9] However, the excessive anti-angiogenic effect of regorafenib can lead to the formation of an anoxic environment within the tumor, thus enhancing the glycolysis process, reducing the therapeutic effect, and long-term use, but also make the tumor prone to drug resistance.[11] On the other hand, due to poor tumor targeting and non-specific distribution in normal tissues, chemotherapy drugs are prone to serious side effects.[12] Therefore, there is an urgent need to develop a regorafenib combination chemotherapy regimen with strong targeting, overcoming drug resistance and low side effects.

YC-1 is a prodrug that could be activated under hypoxic conditions and undergo self-immolation to downregulate HIF-1α.[13,14] Recent studies have shown that YC-1 can also be activated intracellularly by Sulfotransferase 1A1 (SULT1A1) to generate a sulfonation response, resulting in specific killing of tumor cells.[15,16] The action of this drug is characterized by its response to a hypoxic environment, resulting in high synergistic efficacy and significant cytotoxic selectivity, particularly against metabolically active tumor cells in a hypoxic environment.[17] YC-1 was reported that inhibition of HIF-1α suppress triple-negative breast cancer growth and angiogenesis by targeting PlGF/VEGFR1-induced macrophage polarization.[18] In addition, Wang et al has been found that YC-1 can induce cell cycle G1 phase arrest by upregulating $p21^{CIP1/WAP1}$ expression in HCC.[19,20] These studies all suggested that YC-1 has multiple antitumor mechanisms and may be a potential combination drug.

In recent years, with the progress of nanotechnology, the application of self-assembled polymer nanocarriers in drug delivery systems has gained great momentum.[20–22] The nanocarrier system can well overcome the shortcomings of high hydrophobicity of drugs, improve bioavailability, prolong blood circulation time, and achieve better targeting through surface modification.[23–25] Based on these advantages of the nano drug delivery system, it can be well used to load anti-tumor drugs to solve the current clinical problems such as drug resistance, poor targeting and drug side effects. Polylactic acid (PLGA) is an FDA-approved biocompatible and biodegradable polymer that is an effective delivery vehicle for hydrophobic chemotherapy drugs.[26] Poly (ethylene glycol) ylated (PEGylated) nanocarriers have been previously demonstrated to control drug release, promote drug stability in the circulation and reduce non-specific absorption.[27] In addition, the design and development of ligand-conjugated nanoparticles (NPs) allows the nanocarriers to bind specifically to bioactive molecules expressed on tumor cells, further facilitating the active delivery of chemotherapeutic agents to the tumor site.[28]

In solid tumors, due to uncontrolled cell proliferation and abnormal angiogenesis, hypoxia is extremely prevalent. The hypoxic state also exacerbates oxidative stress, prompting cells to generate a large amount of ROS, which accumulate in the tumor microenvironment. Herein, in order to enhance the effect of HCC by alleviating tumor hypoxia and improving the targeting of chemotherapy drugs, we designed a tumor-targeted ROS responsive drug delivery platform to achieve a synergistic treatment of HCC with good therapeutic effect and negligible side effects. As shown in Scheme 1, the hydrophobic chemotherapeutic agent Regorafenib (REG) and the HIF-α inhibitor YC-1 were encapsulated in the Arginine - Glycine - Aspartic acid (RGD)-modified amphiphilic polymer PLGA-TK-PEG as REG/YC-1@PTP-RGD NPs (RYP-RGD NPs). The nanomedicine can identify tumor cells and precisely target HCC regions with the help of RGD peptides. When the nanomaterials reach the tumor tissue, thioketal TK can be specifically cut off by high ROS concentration in the tumor tissue, thus triggering the release of encapsulated REG and YC-1.[24,29,30] Among them, REG can inhibit the formation of neovascularization and play an anti-tumor action, while YC-1 can inhibit the expression of HIF-α, regulate the hypoxia state of tumors, and effectively enhance the anti-tumor efficiency.[31,32] In short, the successful development of the nano drug delivery platform can precisely target the tumor area and control the release of drugs, so that the combination of microenvironment regulation and chemotherapy is effective, which is expected to provide a basis for the treatment of drug-resistant tumors.

Materials and Methods

Materials and Reagents

All chemicals were utilized as supplied unless explicitly purified. Dulbecco's Modified Eagle Medium (DMEM) and fetal bovine serum (FBS) were acquired from Beijing Solarbio Technology Co., Ltd. (China). Additional reagents, including

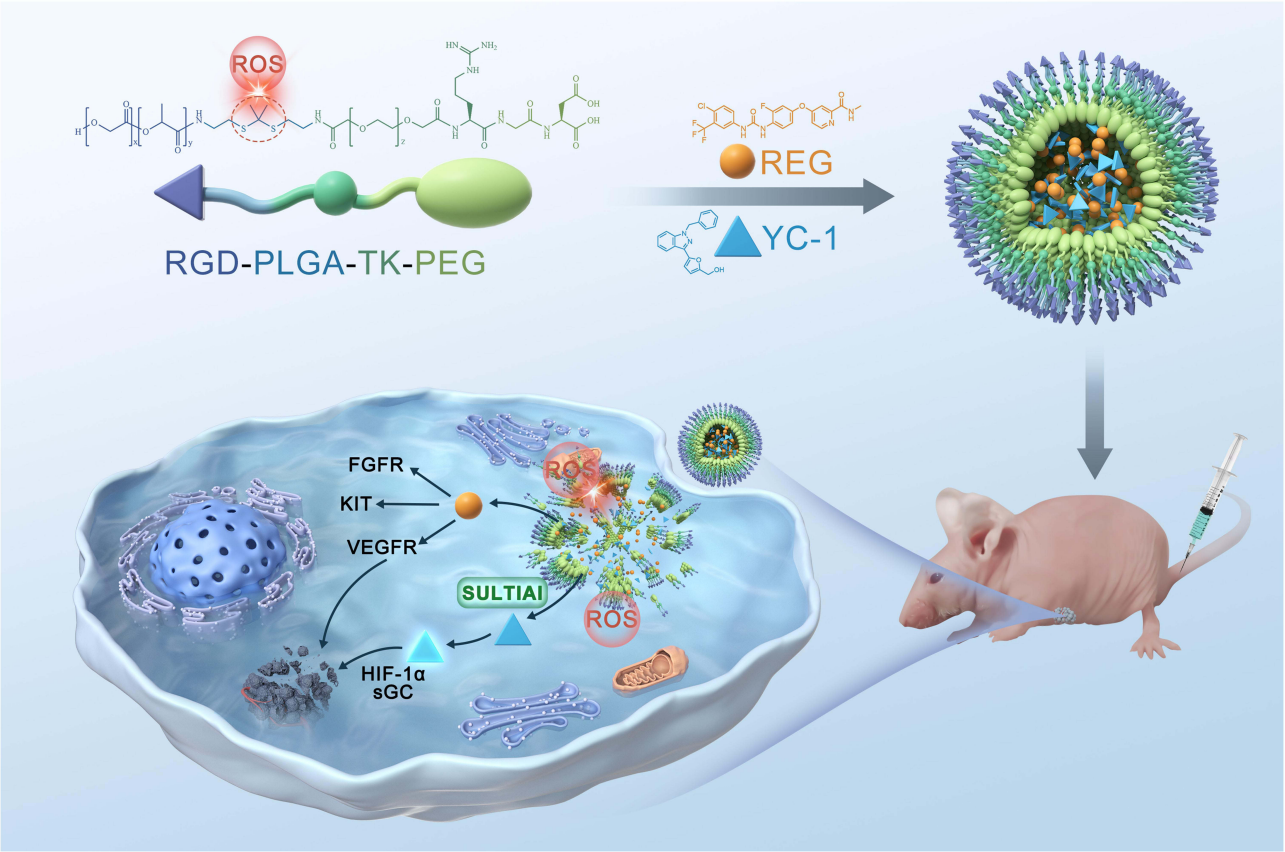

Scheme 1 The synthetic route of biomimetic nanodrugs (RYP-RGD NPs) and its subsequent application in targeted chemotherapy of mice subcutaneous hepatocellular carcinoma tumor model.

ethylenediaminetetraacetic acid (EDTA), Calcein/PI Cell Viability/Cytotoxicity Assay Kit, Hematoxylin-Eosin (H&E) staining kit, Cell Counting Kit-8 (CCK-8), TUNEL apoptosis assay kit, membrane protein extraction kit, and Annexin V-FITC Apoptosis Detection Kit, were sourced from Beyotime Biotechnology Co., Ltd. (China). PLGA-TK-PEG-RGD and PLGA-TK-PEG-NH_2 polymers were obtained from Xi'an Ruixi Biological Technology Co., Ltd. (China). Regorafenib (T1792) and Lificiguat (YC-1, HY-14927) were provided by Shanghai Taoshu Biotechnology Co., Ltd. (China) and MedChemExpress (China), respectively. IR-780 iodide and polycarbonate membranes (220 nm pore size) were purchased from Shanghai Macklin Biochemical Technology Co., Ltd. L02, HepG2, and HCCLM3 cells were purchased from the Type Culture Collection of the Chinese Academy of Sciences (Shanghai, China).

Characterization

The nanoparticles were characterized and analyzed utilizing state-of-the-art instrumentation. Morphological assessment was executed via transmission electron microscopy (TEM) employing an HT 7800 microscope (Hitachi, Japan). Hydrodynamic diameter and ζ-potential determinations were obtained using a Malvern Nano-ZS particle sizer (Malvern Panalytical, UK). Ultraviolet-visible (UV-vis) absorption spectra were recorded with a Shimadzu UV-2700 spectrophotometer (Shimadzu, Japan). For biological assessments, in vivo, fluorescence imaging was conducted on an IVIS Spectrum system (PerkinElmer, USA), and cellular uptake dynamics were examined using a Nikon A1R laser scanning confocal microscope (Nikon, Japan). Structural characterization was achieved through nuclear magnetic resonance (NMR) spectroscopy utilizing a Bruker Avance NEO 600 MHz spectrometer (Bruker Corporation, USA), and drug quantification was performed using an Agilent 1260 Infinity II high-performance liquid chromatography (HPLC) system (Agilent Technologies, USA).

https://doi.org/10.2147/IJN.S518120

Fabrication of RYP-RGD NPs

REG/YC-1@PTP-RGD nanoparticles (RYP-RGD NPs) were synthesized through a self-assembly protocol.[33–35] Briefly, a solution containing 2 mg of regorafenib (REG), 10 mg of YC-1, and 10 mg of PLGA5K-TK-PEG2K-RGD copolymer was prepared by dissolving the components in 1 mL of chloroform, followed by incubation at 37°C for 2 minutes. The organic phase was emulsified by dropwise addition into 5 mL deionized water containing 2% (w/v) polyvinylpyrrolidone (PVP) under magnetic stirring (1,000 rpm). Ultrasonication (4 minutes total duration, 5 s pulse on/5 s pulse off cycles) was applied to generate a homogeneous emulsion. Chloroform was evaporated overnight at 25°C under continuous stirring. The resulting nanoparticle suspension was centrifuged at 15,000 rpm for 10 minutes, followed by two washing cycles with deionized water, and subsequent lyophilization for 24 hours to obtain the final RYP-RGD NPs product. PTP-RGD nanoparticles (PTP-RGD NPs), REG@PTP-RGD nanoparticles (RP-RGD NPs), YC-1@PTP-RGD nanoparticles (YP-RGD NPs), and REG/YC-1@PTP nanoparticles (RYP NPs) were prepared by omitting specific components while maintaining identical synthesis conditions.

The encapsulation efficiency (EE%) and drug loading capacity (DL%) were quantitatively determined using high-performance liquid chromatography (HPLC). For analysis, a 0.5 mL aliquot of the nanoparticle suspension was diluted with deionized water to a final volume of 2 mL.REG and YC-1 concentrations were determined at 268 nm and 328 nm, respectively, using pre-validated calibration curves: REG: $y=25.2x+19.7$ ($R^2=0.999$); YC-1: $y=13.1x+15.9$ ($R^2=0.999$).

Calculations followed: EE% = (Mass of encapsulated drug/Mass of initial drug) ×100%; The drug loading percentage (DL%) is calculated using the formula: DL% = (Mass of encapsulated drug / Mass of nanoparticles) × 100%.

Drug Release Behavior in vitro

The drug release profile was assessed through dialysis methodology. Specifically, 2 mL of RYP-RGD NPs suspension was loaded into a dialysis membrane (MWCO: 3.5 kDa, Beyotime Biotechnology) and immersed in 40 mL of phosphate-buffered saline (PBS, pH 7.4) containing 0.1% (w/v) Tween 80, with or without 10 mM hydrogen peroxide (H_2O_2) supplementation. The system was maintained at 37°C under orbital shaking (60 rpm). At predetermined time intervals (0.5–72 h), 2 mL aliquots of the release medium were collected and replaced with an equal volume of fresh phosphate-buffered saline (PBS). Cumulative release percentages were calculated from UV absorbance values (REG: 268 nm; YC-1: 328 nm) using linear regression equations: REG: $y=20.8x+0.06$ ($R^2=0.999$); YC-1: $y=10.3x+0.09$ ($R^2=0.999$).

Hemolysis Experiments

Whole blood specimens were collected from healthy murine subjects via orbital venous plexus extraction and subsequently subjected to centrifugation at 3,500 rpm for 5 minutes to segregate erythrocyte fractions. The resultant red blood cell (RBC) pellet was rinsed twice with phosphate-buffered saline (PBS) and reconstructed to formulate a 2% (V/V) suspension. Aliquots of the erythrocyte suspensions (0.2 mL) were incubated with phosphate-buffered saline (serving as a negative control), deionized water (employed as a positive control), or PTP-RGD NPs at concentrations spanning from 10 to 500 μg/mL, under a constant thermal environment of 37°C for 4 hours. Post-incubation, the samples were centrifuged at 1,000 rpm for 5 minutes, and the absorbance of the supernatant was quantified spectrophotometrically at a wavelength of 541 nm. Hemolysis rates were subsequently calculated as: Hemolysis rate (%) = $(A_{preparation}-A_{negative})/(A_{Positive}-A_{negative}) \times 100\%$.

In vitro Cytotoxicity Assay

The HepG2, HCCLM3, and LO2 cell lines were seeded in 96-well culture plates at an initial density of 5×10^3 cells per well and permitted to adhere overnight under standard incubation conditions. Subsequently, the cells were subjected to treatment with PTP-RGD NPs at concentrations ranging from 10 to 500 μg/mL for 12 hours. Post-treatment, each well was supplemented with 100 μL of fresh culture medium containing CCK-8 reagent at a 10% (V/V) dilution. Following a 1-hour incubation period at 37°C, absorbance readings were recorded at 450 nm using a microplate reader. Cell viability was quantified as a percentage, calculated by the formula: Cell viability (%) = (OD of the experimental samples / OD of the control) × 100%, with values normalized against untreated control groups.

In vitro Cell Uptake Assay

FITC-Labeled Nanoparticle Preparation: Fluorescein isothiocyanate (FITC; 1 mg) was dissolved in 1 mL of deionized water, followed by centrifugation at 1,000 rpm for 3 minutes to remove any insoluble particulates. The supernatant (20 μL) was mixed with PTP-RGD NPs or PTP NPs (1 mg/mL) and incubated overnight in the dark. Labeled nanoparticles (PR-FITC NPs, PTP-FITC NPs) were purified by centrifugation (15,000 rpm, 5 minutes) and resuspended in PBS.

Cellular Uptake Assay: HepG2, HCCLM3, and LO2 cell lines, each at a density of 1×10^5 cells per plate, were exposed to PR-FITC nanoparticles for 2 hours. Subsequently, the cells were immobilized by treating them with a 4% (w/v) paraformaldehyde solution for 15 minutes at ambient temperature. Following fixation, the cells were stained using DAPI at a dilution of 1:1,000 for 30 minutes and then visualized using fluorescence microscopy. To assess the RGD peptide-mediated active targeting efficacy, HepG2 cells were concurrently incubated with either PR-FITC nanoparticles or PTP-FITC nanoparticles under standardized conditions at 37°C for 2 hours.

Western Blot

Subcellular protein fractions, encompassing both membrane and cytosolic proteins were extracted utilizing a commercially available Membrane and Cytosol Protein Extraction Kit (Solarbio, China). Protein concentrations were determined via a bicinchoninic acid (BCA) assay kit (Epizyme, China). For immunoblotting, protein samples (20μg per lane) were separated on 10% sodium dodecyl sulfate-polyacrylamide gels (SDS-PAGE) and subsequently transferred onto polyvinylidene fluoride (PVDF) membranes with a pore size of 0.45 μm (Millipore). The PVDF membranes were blocked with 5% (w/v) non-fat dry milk in Tris-buffered saline containing Tween-20 (TBST) for 1 hour at an ambient temperature. Following this, the membranes were incubated with primary antibodies: anti-β-tubulin (1:5,000 dilution; Proteintech, USA), anti-SULT1A1 (1:1,000; Abcam, UK), anti-Na^+/K^+-ATPase (1:1,000; Beyotime, China), and anti-HIF-1α (1:1,000; Abcam, UK). Post-washing, the membranes were exposed to horseradish peroxidase (HRP)-conjugated secondary antibodies (1:5,000 dilution; Proteintech, USA) for 1 hour at room temperature. Protein bands were visualized employing an enhanced chemiluminescence substrate kit (Abbkine, USA), adhering to the manufacturer's specified protocol.

In vitro Anti-Tumor Studies

HepG2 and HCCLM3 cells were inoculated at a concentration of 5×10^3 cells per well in 96-well plates and subjected to a 24-hour treatment under various experimental conditions: phosphate-buffered saline (PBS) as the control, free Regorafenib (REG) at concentrations ranging from 1 to 10 μg/mL, free YC-1 at concentrations ranging from 7 to 70 μg/mL, YRP nanoparticles, and RYP-RGD nanoparticles. After the treatment period, cell viability was evaluated utilizing the Cell Counting Kit-8 (CCK-8) assay, adhering to the methodology outlined above. The cell viability can be calculated as follows: First, subtract the absorbance value of the blank control group (Ab) from the absorbance value of the experimental group (As), that is, As - Ab. Then, divide the resulting difference by the difference between the absorbance values of the normal control group and the blank control group (Ac - Ab), namely (As - Ab)÷(Ac - Ab). Finally, multiply the above - mentioned ratio by 100%. In other words, the cell viability = [(As - Ab) / (Ac - Ab)] × 100%.

In this experimental design, the optical density values of the treatment group, control group, and blank control group at a wavelength of 450 nanometers are denoted as As, Ac, and Ab respectively.

Quantitative Analysis Was Performed by Flow Cytometry

HepG2 cells were seeded at a density of 5×10^5 cells per well in 6-well plates and subjected to the following treatments for 24 hours: free regorafenib (REG; 3 μg/mL), YRP NPs, RYP-RGD NPs, free YC-1 (21 μg/mL), or equivalent nanoparticle formulations at corresponding concentrations. Post-treatment, the cells were harvested using an EDTA-free trypsin solution, dual-labeled with Annexin V-FITC and propidium iodide (PI) via a commercial apoptosis detection kit (Beyotime, China), and subsequently analyzed using flow cytometry (BD FACSCanto II, USA).

Qualitative Analysis Was Performed by Fluorescence Imaging

In adherence to established treatment protocols, HepG2 cells were subjected to incubation with a staining solution comprising Calcein-AM and propidium iodide (PI), derived from a commercially available viability/cytotoxicity assay kit (Beyotime, China), for 30 minutes under conditions shielded from light exposure. Fluorescence microscopy images were captured utilizing an inverted fluorescence microscope (Nikon Eclipse Ti, Japan) fitted with suitable filter configurations. A quantitative assessment of live-to-dead cell ratios was conducted utilizing ImageJ software (version 1.53, National Institutes of Health, USA), employing standardized processing parameters.

Animals and Tumor Model

All animal experimental protocols were rigorously reviewed and approved by the Institutional Animal Care and Use Committee (IACUC) of Zhengzhou University (Approval No. ZZU-LAC2023082204), adhering to national guidelines for the ethical care and utilization of laboratory animals. Female BALB/c nude mice, aged 4–6 weeks, were procured from Beijing Huafukang Biotechnology Co., Ltd. (China) and maintained under specific pathogen-free (SPF) conditions. For the establishment of tumor xenografts, the mice were subcutaneously inoculated with HepG2 cell suspensions (1×10^7 cells in 100 μL phosphate-buffered saline, PBS) into the right dorsal flank utilizing a 27-gauge needle.

In vivo Biodistribution of RYP-RGD NPs

Mice harboring xenograft tumors with volumes nearing 400 mm^3 were randomly assigned to treatment cohorts and received intravenous injections of either IR780@PTP nanoparticles or IR780@PR nanoparticles via the tail vein. In vivo, fluorescence imaging was conducted at specified temporal intervals (0, 2, 4, 8, 10,12, and 24 hours post-administration) utilizing the IVIS Spectrum imaging system (PerkinElmer, USA), adhering to uniform imaging settings. After euthanasia was performed following approved ethical guidelines, tumors and principal organs (including the heart, liver, spleen, lungs, and kidneys) were excised for ex vivo fluorescence imaging and quantitative analytical procedures.

In vivo Antitumor Effect and Biosafety of RYP-RGD NPs

Mice were randomly allocated to five experimental cohorts (n = 10 per cohort) as follows: (1) phosphate-buffered saline (PBS) control, (2) free regorafenib (REG), (3) free YC-1, (4) REG/YC-1@PTP nanoparticles (RYP NPs), and (5) RYP-RGD nanoparticles (RYP-RGD NPs). Treatment solutions (100 μL injection volume), comprising REG at a concentration of 0.2 mg/mL and YC-1 at 1.4 mg/mL, were administered intravenously via the tail vein at 48-hour intervals for a total of five treatment cycles. Tumor volume ($V = 0.5 \times \text{length} \times \text{width}^2$) and body weight were monitored over 15 days. Tumors were subjected to hematoxylin and eosin (H&E) staining, Ki-67 immunohistochemical analysis, and terminal deoxynucleotidyl transferase dUTP nick-end labeling (TUNEL) apoptosis assay. Blood samples were analyzed for hepatic and renal function markers (alanine aminotransferase [ALT], aspartate aminotransferase [AST], albumin [ALB], uric acid [UA], urea [UREA], creatinine [CREA]) and hematological parameters (white blood cells [WBC], red blood cells [RBC], platelets [PLT]).

Statistical Analysis

Statistical analyses were performed using GraphPad Prism version 9.0.0 (GraphPad Software,LLC). All quantitative data are presented as mean ± standard deviation (SD), derived from three biologically independent replicates. Statistical assessments were conducted employing Student's *t*-test for pairwise comparisons between two groups, and one-way analysis of variance (ANOVA) supplemented by Tukey's post hoc test for multi-group comparisons. The markers for statistical relevance were delineated thusly: $^*P < 0.05$, $^{**}P < 0.01$, and $^{***}P < 0.001$.

Results and Discussion

Synthesis and Characterization of RYP-RGD NPs

Figure 1A shows that the small molecule drugs REG and YC-1 have typical hydrophobic structures, which often leads to poor stability and low bioavailability in clinical applications. Therefore, encapsulation with amphiphilic polymer carriers can effectively improve their water solubility and increase drug circulation time and utilization. In this study, an

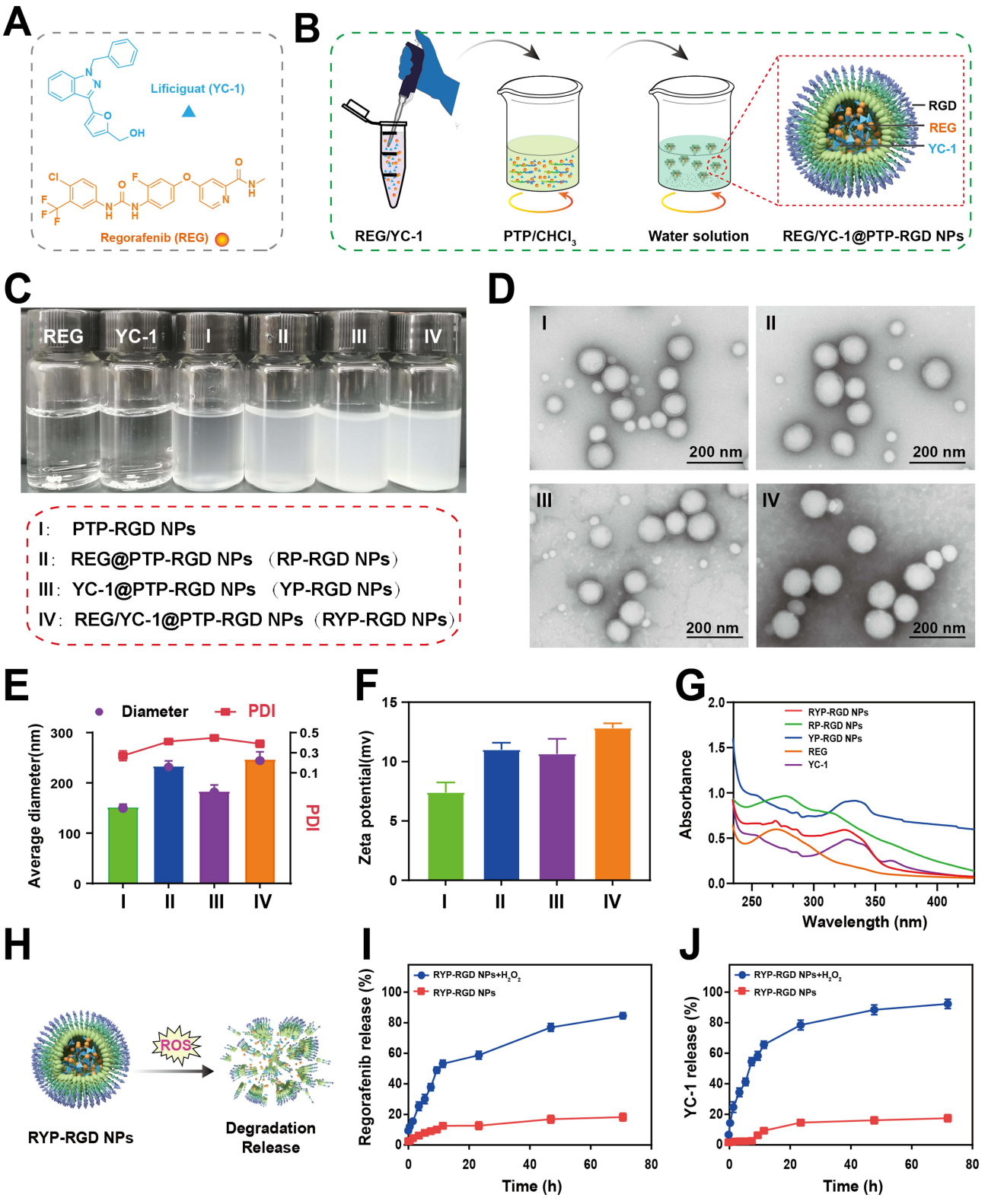

Figure 1 Synthesis and characterization of the RYP-RGD NPs. (**A**) The formula structure of YC-1 and REG. (**B**) Schematic illustration of the fabrication of RYP-RGD NPs. (**C**) The solubility of REG, YC-1, RP-RGD NPs, YP-RGD NPs, and RYP-RGD NPs in PBS buffer. (**D**) TEM images of (**I**) PTP-RGD NPs, II: RP-RGD NPs, III: YP-RGD NPs, and IV: RYP-RGD NPs. (**E**) Average diameter of PTP-RGD NPs, RP-RGD NPs, YP-RGD NPs, and RYP-RGD NPs. (**F**) Zeta potential of PTP-RGD NPs, RP-RGD NPs, YP-RGD NPs, and RYP-RGD NPs. (**G**) UV-Vis absorption spectra of YC-1, REG, RP-RGD NPs, YP-RGD NPs, and RYP-RGD NPs. (**H**) Schematic diagram of RYP-RGD NPs cleavage under the action of ROS. (**I**) The REG release of RYP-RGD NPs under different conditions. (**J**) The YC-1 release from RYP-RGD NPs under different conditions.

https://doi.org/10.2147/IJN.S518120

amphiphilic polymer (PLGA-TK-PEG-RGD) was used as a drug carrier, which was formed by linking PLGA, PEG and RGD to ketothiols (TK) with ROS-responsive fracture characteristics. ^{1}H NMR spectra showed that the proton resonance of the PLGA main chain was identified as a signal source of about 1.24, 1.71 and 2.54 ppm, and the formation peaks of mPEG methylmethylate and terminal methylformyl matrix were located at 4.12 and 3.78 ppm, respectively (Figure S1). Moreover, successful grafting of RGD was demonstrated between 7.0 and 9.5 ppm (Figure S2). As shown in Figure 1B, RYP-RGD NPs were prepared by typical ultrasonic emulsification process.[33–35] The nanodrugs are composed of three parts: internal hydrophobic drugs (REG and YC-1), external PLGA-TK-PEG and RGD of end-group targeting polypeptide. Through the coating of amphiphilic polymers, we found that the solution state of the drug changed significantly. As shown in Figure 1C, REG and YC-1 had low solubility in water and appeared as white precipitation. In stark contrast, the nanodrugs loaded with either single or double drugs can show good water dispersion and stability, which is very important for the blood circulation and biosafety of drugs.

Subsequently, the morphology of nanodrugs were characterized by Transmission electron microscope (TEM). As shown in Figure 1D, the prepared nanodrugs have a spherical structure, relatively uniform and good dispersion, with a particle size of about 120 nm. Moreover, compared with PTP NPs containing no drug, the morphology of PTP-RGD NPs containing either single drug or double drug has no obvious change. It can be seen from Figure 1E, the average particle sizes of PTP-RGD NPs, RP-RGD NPs, YP-RGD NPs, and RYP-RGD NPs are 148.12 nm, 231.71 nm, 189.56 nm, and 242.81 nm, respectively. Compared with PTP-RGD NPs, the average particle size of the nanodrug is increased to a certain extent, and it is worth mentioning that the particle size of the nanodrug encapsulated by REG is relatively large (Figure 1E). As shown in Figure 1F, the prepared PTP-RGD NPs, RP-RGD NPs, YP-RGD NPs, and RYP-RGD NPs were sent for zeta potential analysis, with the results being 7.41 mV, 11 mV, 10.66 mV, and 12.83 mV, respectively. Zeta potential analysis found that drug encapsulating did not significantly change the surface properties of nanomaterials, mainly because hydrophobic small molecule drugs are mainly wrapped in the inside of nanoparticles and do not affect the external properties. The successful encapsulation of REG and YC-1 is also verified by UV-vis spectra. It can be seen from Figure 1G that RP-RGD NPs and RYP-RGD NPs both have characteristic peaks of REG at 268nm. Similarly, YP-RGD NPs and RYP-RGD NPs both have the characteristic absorption peak of YC-1 at 328 nm. These results mark the successful encapsulation of REG and YC-1 either individually or jointly. The drug loading capacity and encapsulation rate of REG and YC-1 were also calculated by HPLC-UV (Figures S3–S5). The drug loading capacity of RP-RGD NPs and RYP-RGD NPs for REG were 10.8% and 8%, and the encapsulation rate were 47% and 63%, respectively. In contrast, the drug loading of YP-RGD NPs and RYP-RGD NPs for YC-1 was 38.3% and 51.6%, and the encapsulation rate was 57.8% and 86.8%, respectively (Table S1). To evaluate the stability of the prepared nanocarriers, their size and polydispersity Index (PDI) were monitored for 14 days at different time points. As shown in Figures S6 and S7, there were no significant changes in size and morphology when RYP-RGD NPs were stored in PBS for 14 days, suggesting enhanced stability of the prepared nanoparticles.

The tumor microenvironment has a high concentration of ROS, so the thioketal bond (TK) contained in the nanodrug can be breakage in a responsive manner in the tumor site (Figure 1H). For this purpose, the release kinetics of RYP-RGD NPs were determined in the presence and absence of ROS. As shown in Figure 1I and J, REG in RP-RGD NPs released only 18.67% of the REG in PBS within 72 hours and 30.14% of the REG within 6 hours in the presence of ROS. Similarly, YP-RGD NPs released only 16.19% of the originally encapsulated YC-1 within 72 hours in PBS, whereas in a ROS environment, the release rate reached 90.52% within 72 hours. The results show that RYP-RGD NPs can be destroyed by ROS, which makes the originally tight micelles loose and porous, resulting in rapid release of REG and PTP, and they have similar release behaviors. As shown in Figure S8, the cytotoxicity test showed no noticeable killing effect on normal liver cells and cancer cells. Moreover, we also monitored the blood compatibility of prepared PTP-RGD NPs. The results show that even with treatment of PTP-RGD NPs at 500 μg/mL, there is almost no hemolysis, proving the biosafety of the nanodrugs (Figure S9).

The Anti-Tumor Effect of RYP-RGD NPs in vitro

RGD polypeptide (Arg-Gly-Asp) is a polypeptide sequence that exists in a variety of biological extracellular matrix, which can specifically recognize and bind to tumor cell surface integrins to achieve targeted therapy of tumor cells.[36,37]

To investigate the specificity of nanodrug targeting human hepatocytes, we used LSCM to observe the uptake of FITC-labeled PTP-RGD NPs by HCC cells (HepG2 and HCCLM-3) and normal LO2 hepatocytes. After phagocytosis of FITC-labeled PTP-RGD NPs, the fluorescence intensities detected in HepG2 and HCCLM-3 cells were 225.50 FIU and 209.21 FIU, respectively, while the fluorescence intensity in LO2 cells was only 76.65 FIU. The results showed that the green fluorescence intensity in liver cancer cells was significantly higher than that in LO2 cells, indicating that RGD-modified targeted nanodrugs showed excellent selectivity to liver cancer cells, confirming its good tumor targeting effect (Figure 2A and B). At the same time, we also investigated the effect of RGD modification on the targeting of nanomaterials administration by co-culturing RGD-FITC, PTP-FITC NPs and PR-FITC NPs with HepG2 cells. We can observe that in the three groups of HepG2 cells, the intracellular fluorescence intensity in the RGD-FITC, PTP-RGD NPs group is 196.32FIU and 234.54 FIU respectively, while the fluorescence intensity in the PTP NPs group is only 109.66 FIU (Figures 2C, D and S10). These results showed that RGD modification could significantly improve the phagocytoses of nanoparticles by HepG2, again demonstrating its good targeting.

To illustrate the therapeutic effect of the prepared ROS-responsive nanodrugs, we first detected the ROS levels of different cell types using fluorescence probes. Figure S11 showed that hepatocellular carcinoma cells have a higher level of ROS than normal liver cells, which is very conducive to the selective drug release of ROS-responsive nanocarriers. We then evaluated the in vitro toxicity of RYP-RGD NPs on hepatocellular carcinoma cells, and here we selected HepG2 and HCCLM-3 cells as models for the relevant evaluation (Figures 2E and S12). HepG2 cells treated with different concentrations of REG, YC-1, RYP NPs and RYP-RGD NPs showed concentration-dependent cytotoxicity. Notably, RYP NPs and RYP-RGD NPs showed more pronounced cytotoxicity than equivalent amounts of REG. Also, and more interestingly, when the cells were treated with a different material containing 10 μg/mL REG, RYP-RGD NPs led to about 76.83% cell death, much higher than REG (42.17%) and RYP NPs (44.6%). Subsequently, we analyzed the related mechanism of YC-1 enhancing the efficacy of REG tumor therapy. YC-1 is an inhibitor of hypoxia inducible factor-1α (HIF-1α), which can improve tumor hypoxia and improve tumor drug resistance. Recent studies have shown that SULT1A1 enzyme can activate YC-1 compounds in cells, thus showing good anti-tumor effects.[38,39] The drug carrier can efficiently transport YC-1 to the interior of the cell, accumulate in large quantities, and then activated by SULT1A1 to play a role (Figure 2F). To this end, the expression of SULT1A1 in cells was first investigated. As shown in Figure S13, SULT1A1 was mainly expressed in the cytoplasm, but not on the cell membrane. Then, we investigated the effect of RYP-RGD NPs on SULT1A1 expression. As shown in Figures 2G and S14, SULT1A1 expression in the control group, YC-1 group, RP-RGD NPs group and RYP-RGD NPs group. The results showed that the addition of YC-1 decreased the expression of SULT1A1, further enhanced by nanomaterials' encapsulation. These results indicate that our nanocarrier system accelerates the depletion of SULT1A1, thereby affecting its sulfonation process and promoting the metabolism of YC-1, thereby enabling it to rapidly exert anti-tumor effects. Live cell/dead cell fluorescence staining also demonstrated that RYP-RGD NPs had a good therapeutic effect on tumor cells (Figures 2H and I). Quantitative flow cytometry showed that the apoptosis rate induced by RYP-RGD NPs at the same REG concentration was 65.1%. In the pure drug group, the rate was only 18.3% (Figure 2J). This result was mainly due to the targeting of RYP-RGD NPs, which increased the concentration of intracellular REG&YC-1 and significantly enhanced the effect of chemotherapy.

In vivo Biodistribution and Tumor Targeting

The body's body fluids and immune system easily clear traditional drugs, resulting in short blood circulation times. Previous study found that PEG-modified nanoparticles can significantly improve the blood circulation time of nanoparticles, and this result is expected to enhance tumor uptake and pharmacokinetics after the addition of RGD. Then, we evaluated the tissue distribution of RYP-RGD NPs in vivo. Firstly, tumor cells were injected in the axilla of mice to form hormonal mice. Secondly, IR780 coated with PTP or PTP-RGD were intravenously injected into the nude mice. Finally, in vivo IVIS imaging was performed to monitor the biodistribution of IR780@PTP-RGD NPs. As depicted in Figure 3A and B, we found that IR780@PTP-RGD NPs remain in the blood longer and decline more slowly. After 48 hours, the mice were sacrificed and the tumor, heart, liver, spleen, lung and kidney were also imaged to detect fluorescence intensity. The results supported that the fluorescence intensity of IR780@PTP-RGD NPs at the tumor site was higher than IR780@PTP NPs (Figure 3C and D), reflecting PTP-RGD NPs have better tumor targeting.

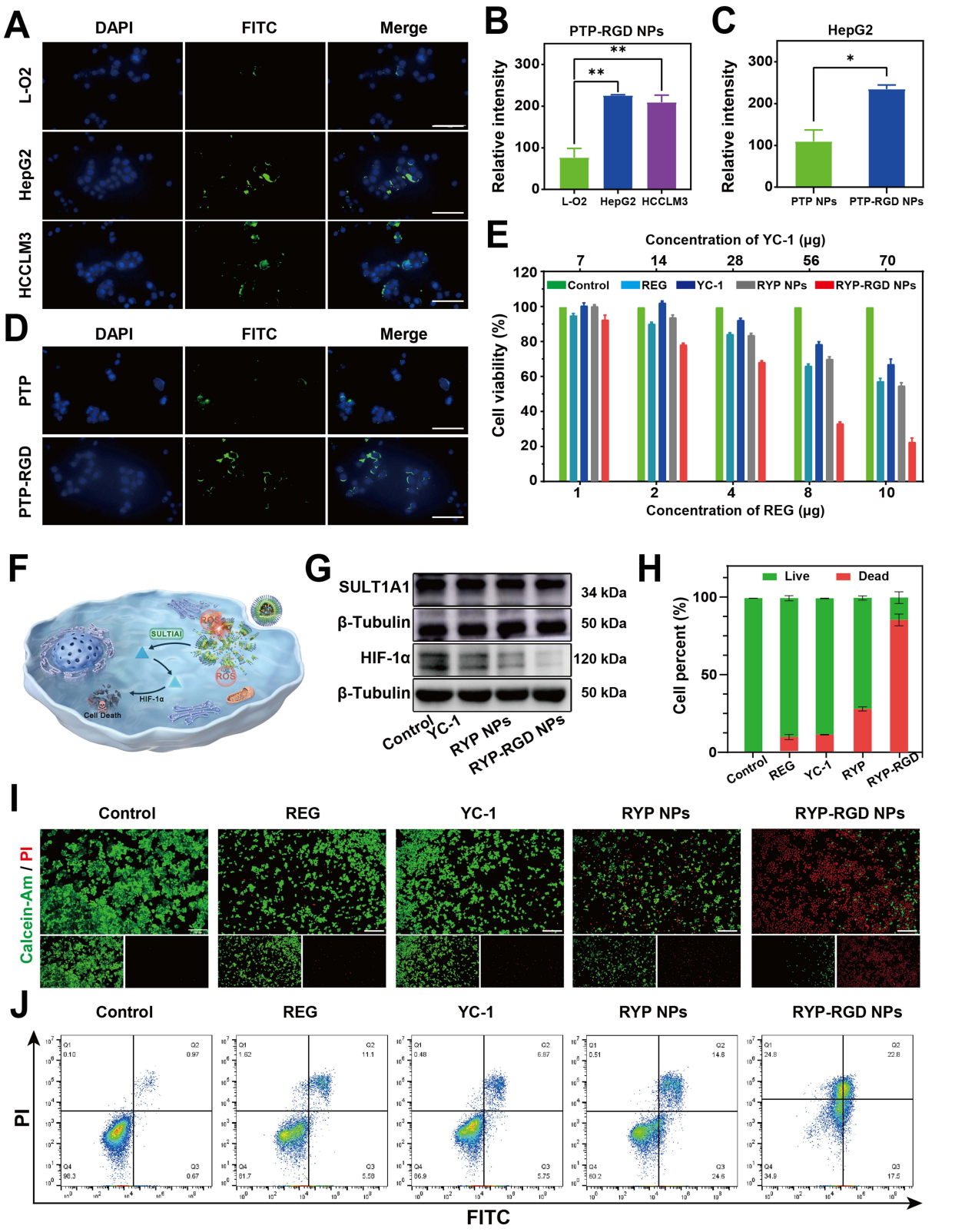

Figure 2 Specific uptake and in vitro anti-tumor activity of RYP-RGD NPs. (**A**) Fluorescence images and the relevant semi-quantitative analysis, Scale bar: 100 μm. (**B**) of LO2, HCCLM3, and HepG2 cells incubated with PTP-RGD NPs for 6 h targeting cancer cells. (**C**) Fluorescence images and (**D**) the relevant semi-quantitative analysis displayed the tumor targeting of PTP-FITC NPs and PR-FITC NPs after incubation with HepG2 cells for 2 h, Scale bar: 100 μm. (**E**) Cell viability of HepG2 treated with different concentrations of REG/YC-1. (**F**) Mechanism of SULT1A1 activation by YC-1. (**G**) The expression of SULT1A1, β-Action, and HIF-1α under different treatments. (**H**) The percentage of live and dead cells under different conditions. (**I**) Fluorescence images of HepG2 cells stained with Calcein-AM and PI after treatment with PBS, REG, YC-1, RYP NPs, and RYP-RGD NPs for 24 h. Green and red fluorescence represent live cells and dead cells, respectively. Scale bar: 100 μm. (**J**) Flow cytometry of HepG2 treated with PBS, REG, YC-1, RYP NPs, and RYP-RGD NPs for 24 h. The values are presented by mean value ± SD. (n=6, *: $p < 0.05$, **: $p < 0.01$).

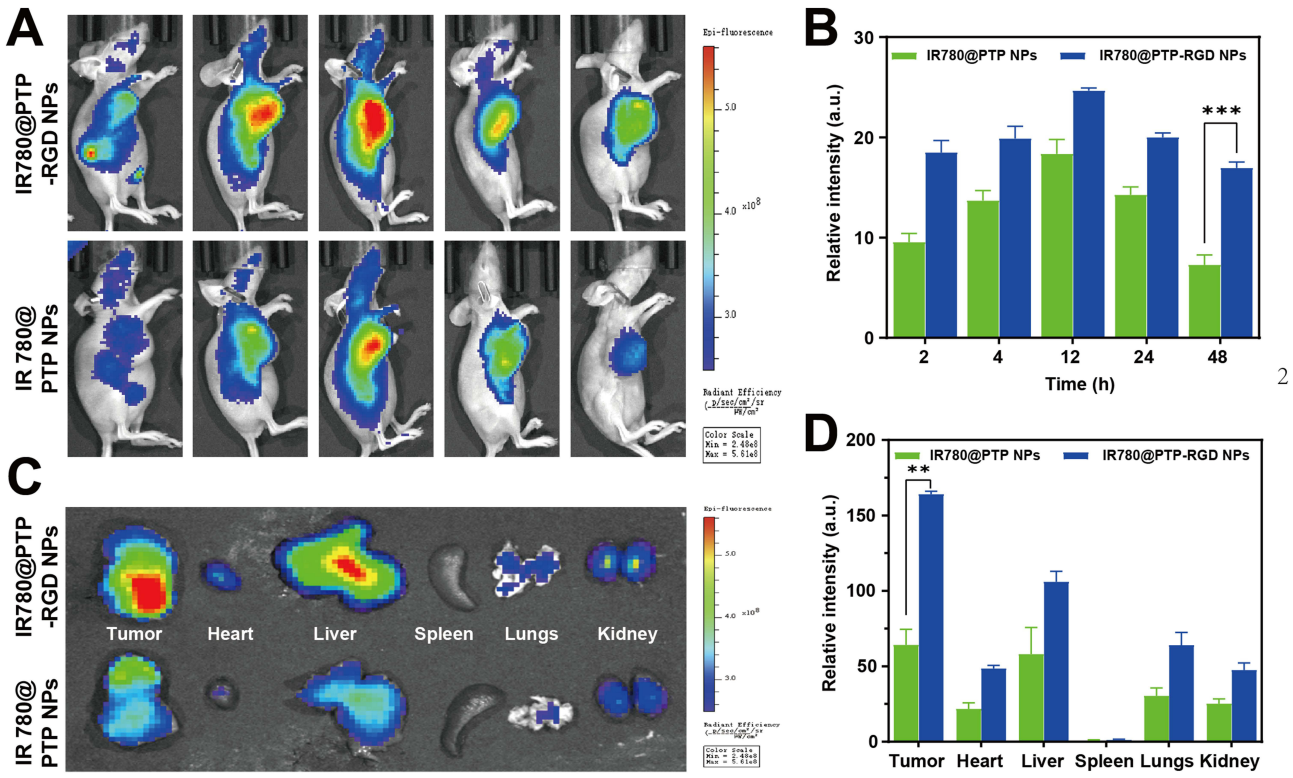

Figure 3 Tumor targeting and tissue distribution of RYP-RGD NPs in vivo. (**A**) In vivo IVIS imaging was performed to monitor the biodistribution of IR780@PTP-RGD NPs on subcutaneous tumor mice model (n = 4). Mice were intravenously injected with IR780@PTP NPs (IR780, 1.5 mg/kg) or IR780@PTP-RGD NPs and the fluorescence images were obtained at 2, 4, 12, 24 and 48 h post injection. (**B**) The relative mean fluorescent intensity changes of IR780@PTP NPs and IR780@PTP-RGD NPs in vivo. (**C**) Ex vivo IVIS imaging was used to examine the IR780 FL signals of major organs and tumor to further study the biodistribution of the nanoparticles, after the mice were sacrificed at 48 hours post injection. (**D**) Semiquantitative analysis the relative intensity of IR780 of major organs and tumor. The data are shown as mean ± SD (n = 5, **, $p < 0.01$; ***, $p < 0.001$).

Anti-Tumor Effect of RYP-RGD NPs in vivo

Given the promising in vitro anti-tumor activity of RYP-RGD NPs, we decided to assess the in vivo therapeutic potential of targeted nanodrugs against hepatocellular carcinoma. To assess the therapeutic effectiveness of RYP-RGD NPs on hepatocellular carcinoma, human HepG2 cells were subcutaneously injected into Balb/c-nude mice using the well-established hepatocellular carcinoma transplantation model. Initially, mice with a right hind limb HepG2 tumor received intravenous injections of PBS, REG, YC-1, RYP NPs, and RYP-RGD NPs at the same drug concentration (Figure 4A). Visually, Figure 4B demonstrated that RYP-RGD NPs had a more significant therapeutic impact than the other groups. The RYP-RGD NPs group had a significantly greater therapeutic impact than the RYP NPs group. This could be because Arg-Gly-Asp (RGD) peptide may enhance the capacity of drugs to target tumors. Simultaneously, RYP-RGD NPs demonstrated longer blood circulation times, enhanced drug release over time in the tumor's weakly acidic microenvironment, and accelerated tumor cell death. By tracking the mice's body weight and tumor volume, it was discovered that the RYP-RGD NPs group significantly reduced tumor growth on Day 15 in comparison to the PBS group and the REG-free treatment group (Figure 4C–E). Moreover, the tumor inhibition rate of REG, YC-1, RYP NPs and RYP-RGD NPs were 22.1%, 24.7%, 38.5%, and 64.4%, respectively, which indicates the combined therapy could significantly improve the anti-tumor efficiency (Figure S15). The tumor tissue sections from each group were then stained with H&E, TUNEL, and Ki67 to assess the tumor tissues' apoptosis, proliferation, and necrosis. The most severe tumor necrosis and apoptosis occurred in mice treated with RYP-RGD NPs, as seen in Figure 4F–H. However, there was less necrosis or apoptosis in the pure REG or YC-1 group, confirming once more that PTP-RGD NPs improved the anticancer impact of REG and YC-1. Moreover, the CD31 immunofluorescence staining results of the tumor mass in Figure S16 showed that compared with free REG, RYP-RGD has a higher vascular inhibitory effect, which indicates that these prepared nanodrugs can also inhibit the proliferation of tumor cells by inhibiting angiogenesis. According to the findings, RYP-RGD NPs may be employed as a new biomimetic nanodrug delivery system to treat liver cancer.

https://doi.org/10.2147/IJN.S518120

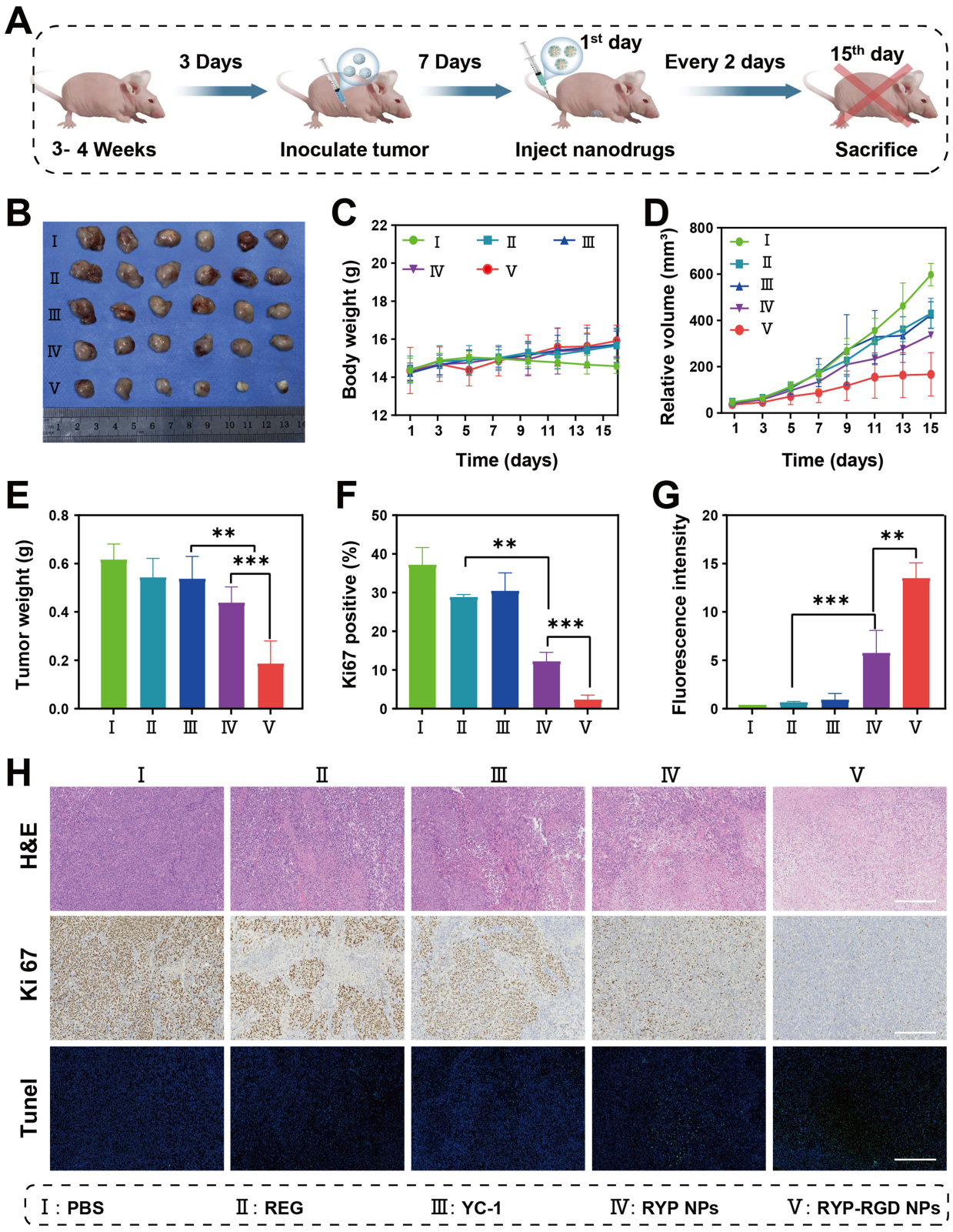

Figure 4 The therapeutic effect of RYP-RGD NPs on HepG2 tumor model mice. (**A**) Schematic diagram of the antitumor treatment on subcutaneous xenograft models. Tumor-bearing mice (n = 8) with a volume of about 100 mm^3 received i.v. Injection of the indicated drugs every two days four times. (**B**) The images of harvested tumors at 15 days post-injection of PBS, REG, YC-1, RYP NPs, and RYP-RGD NPs. (**C**) The body weight of mice treated with PBS, REG, YC-1, RYP NPs, and RYP-RGD NPs. (**D**) The tumor relative volume of mice treated with PBS, REG, YC-1, RYP NPs, and RYP-RGD NPs. (**E**) The tumor weight of mice treated with PBS, REG, YC-1, RYP NPs, and RYP-RGD NPs. (**F**) The relative percentage of Ki67 positive area in subcutaneous tumors. (**G**) Semiquantitative analysis of the fluorescence intensity of TUNEL staining in subcutaneous tumors. (**H**) HE, Ki67 and TUNEL staining of subcutaneous tumors treated with PBS, REG, YC-1, RYP NPs, and RYP-RGD NPs, Scale bar: 50 μm. (**, $p < 0.01$; ***, $p < 0.001$).

 https://doi.org/10.2147/IJN.S518120

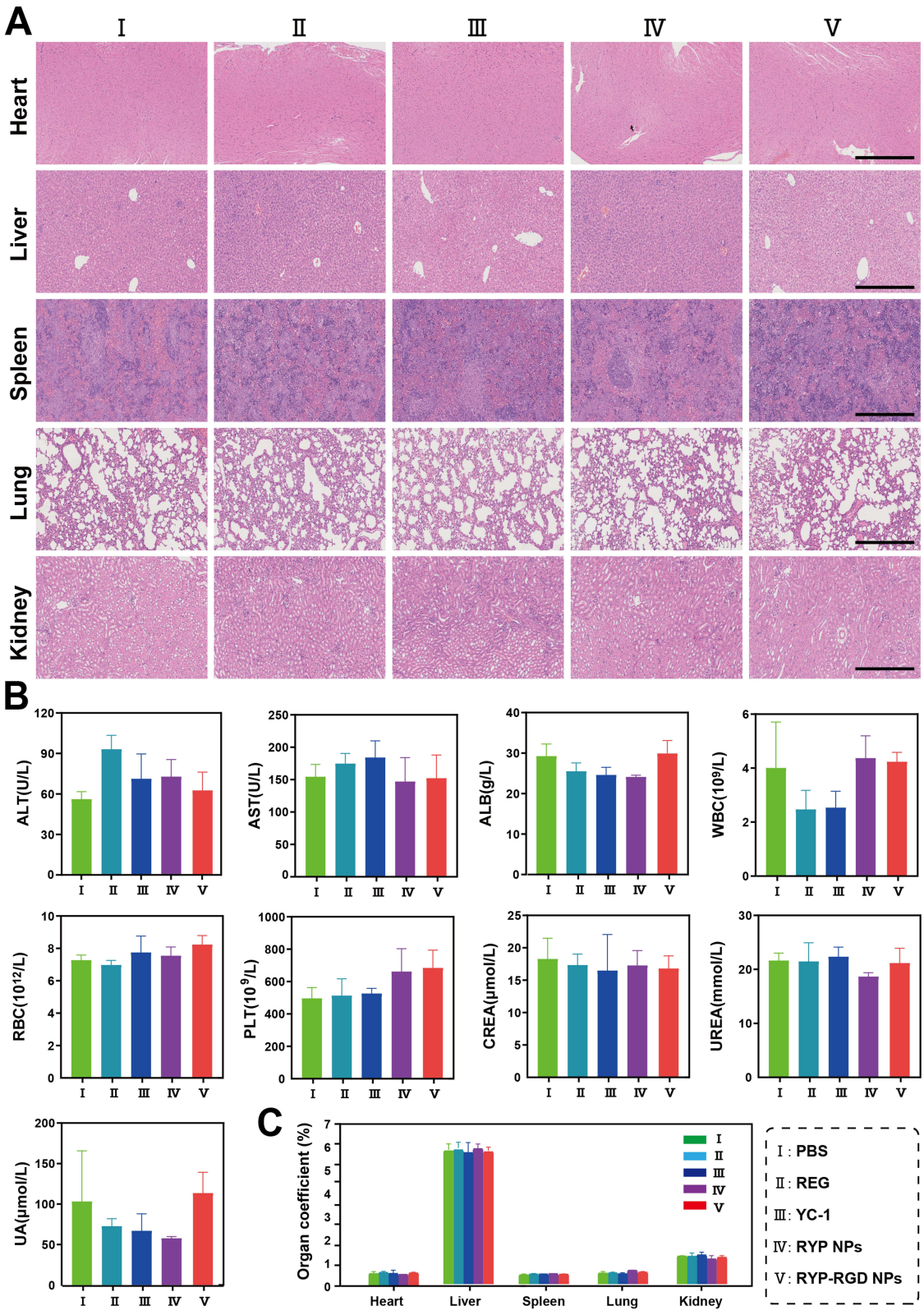

Figure 5 The biosafety of RYP-RGD NPs in vivo. (**A**) H&E histological staining of exercise organic (heart, liver, spleen, lung, and kidney) slices for PBS, REG, YC-1, RYP NPs, and RYP-RGD NPs treatment groups (left to right), respectively. Scale bar = 50 μm. (**B**) Liver function (ALT, AST: alanine aminotransferase, ALB), blood biochemistry analysis (WBC: white blood cells, RBC: red blood cells, PLT: platelets), and kidney function (CREA: creatinine, UREA: urea, UA: uric acid) in mouse serum after treatments with PBS, REG, YC-1, RYP NPs, and RYP-RGD NPs. (**C**) Organ indexes of the heart, liver, spleen, lung and kidney in various groups.

https://doi.org/10.2147/IJN.S518120

The Biosafety of RYP-RGD NPs in vivo

The produced biomimetic nanodrug delivery technology has already been shown to exhibit strong anticancer effects both in vivo and in vitro. Furthermore, neither normal nor liver cancer cells appear to be harmed by PTP-RGD NPs. Tumor patients' fluid circulation differs from that of healthy people, nevertheless. Thus, more research was done on the biosafety of RYP-RGD NPs in healthy tissues and organs. H&E staining of the heart, liver, spleen, lung, and kidney revealed no discernible damage to any of the major organs in each group, as seen in Figure 5A. Furthermore, mice's biochemical blood indices were examined. A number of significant physical health indicators were examined, along with blood routines, liver and kidney functions, and other tests. There was no discernible change between the control group and the RYP-RGD NPs group in Figure 5B. Moreover, compared with the control group, there were no significant differences in the organ indexes of the heart, liver, spleen, lung and kidney in the experimental group, indicating that nanodrugs administered by intravenous injection were not sufficient to cause organ damage in mice at the current dose (Figure 5C). According to the aforementioned findings, RYP-RGD NPs exhibited excellent biosafety in vivo, virtually no harm to healthy tissues, and a wide range of potential clinical uses.

Conclusion

In summary, we successfully constructed and validated ROS-sensitive RYP-RGD NPs in this study. With the incorporation of RGD peptide modification and TK structure, this drug delivery nanosystem has better targeting ability to the tumor and is capable of cleaving and releasing the drug precisely in the ROS-rich environment of the liver cancer. Moreover, YC-1 can effectively reduce the expression of hypoxic factor HIF-1α, alleviate the hypoxic environment generated by REG after drug release, and perfectly combine the two to form a synergistic anticancer effect. Taken together, the RYP-RGD NPs provide a novel strategy for enhancing the precision of first-line clinical medication treatment of HCC. However, this study still has some limitations. For instance, the specific details of the synergistic mechanism between regorafenib and YC-1 and the associated signaling pathways have not been fully elucidated. Nevertheless, this combined tumor therapy strategy based on nanomaterials that regulates the tumor microenvironment will provide new approaches for tumor treatment.

Acknowledgments

This work was financially supported by the National Natural Science Foundation of China (No. 81901808, 82172944), Henan Provincial Natural Science Foundation (232300420041), Henan Province health science and technology innovation talent training project (JQRC2024011). Joint Project of Henan Provincial Science and Technology Research and Development Plan (No. 232301420035, 232102311048). We also thank the Translational Medicine Center of the First Affiliated Hospital of Zhengzhou University for providing the experimental platform. This paper has been uploaded to [ResearchGate] as a preprint: [https://www.researchgate.net/publication/387192514_Ros-Responsive_Nanosystem_Targeted_Co-Delivery_YC-1_and_Regorafenib_Alleviating_Hypoxia_to_Enhancing_Hepatocellular_Carcinoma_Therapy]

Author Contributions

All authors made a significant contribution to the work reported, whether that is in the conception, study design, execution, acquisition of data, analysis and interpretation, or in all these areas; took part in drafting, revising or critically reviewing the article; gave final approval of the version to be published; have agreed on the journal to which the article has been submitted; and agree to be accountable for all aspects of the work.

Disclosure

The authors report no conflicts of interest in this work.

References

1. Bray F, Laversanne M, Sung H, et al. Global cancer statistics 2022: GLOBOCAN estimates of incidence and mortality worldwide for 36 cancers in 185 countries. *CA Cancer J Clin*. 2024;74(3):229–263. doi:10.3322/caac.21834

2. Dasgupta P, Henshaw C, Youlden DR, Clark PJ, Aitken JF, Baade PD. Global trends in incidence rates of primary adult liver cancers: a systematic review and meta-analysis. *Front Oncol*. 2020;10:171. doi:10.3389/fonc.2020.00171
3. Gabutti A, Bhoori S, Cascella T, Bongini M. Hepatocellular carcinoma recurrence after liver transplantation. *Oncology*. 2020;34(3).
4. Tabrizian P, Jibara G, Shrager B, Schwartz M, Roayaie S. Recurrence of hepatocellular cancer after resection: patterns, treatments, and prognosis. *Ann Surg*. 2015;261(5):947–955. doi:10.1097/sla.0000000000000710
5. Lee S, Kim H, Ji Y, et al. Evaluation of hepatic toxicity after repeated stereotactic body radiation therapy for recurrent hepatocellular carcinoma using deformable image registration. *Sci Rep*. 2018;8(1):16224. doi:10.1038/s41598-018-34676-1
6. Bruix J, Gores GJ, Mazzaferro V. Hepatocellular carcinoma: clinical frontiers and perspectives. *Gut*. 2014;63(5):844–855. doi:10.1136/gutjnl-2013-306627
7. Raoul JL, Kudo M, Finn RS, Edeline J, Reig M, Galle PR. Systemic therapy for intermediate and advanced hepatocellular carcinoma: sorafenib and beyond. *Cancer Treat Rev*. 2018;68:16–24. doi:10.1016/j.ctrv.2018.05.006
8. Pang R, Poon RT. Angiogenesis and antiangiogenic therapy in hepatocellular carcinoma. *Cancer Lett*. 2006;242(2):151–167. doi:10.1016/j.canlet.2006.01.008
9. Ettrich TJ, Seufferlein T. Regorafenib. *Recent Results Cancer Res*. 2018;211:45–56. doi:10.1007/978-3-319-91442-8_3
10. Wilhelm SM, Dumas J, Adnane L, et al. Regorafenib (BAY 73-4506): a new oral multikinase inhibitor of angiogenic, stromal and oncogenic receptor tyrosine kinases with potent preclinical antitumor activity. *Int J Cancer*. 2011;129(1):245–255. doi:10.1002/ijc.25864
11. Ladd AD, Duarte S, Sahin I, Zarrinpar A. Mechanisms of drug resistance in HCC. *Hepatology*. 2024;79(4):926–940. doi:10.1097/hep.0000000000000237
12. Li M, Su Y, Zhang F, et al. A dual-targeting reconstituted high density lipoprotein leveraging the synergy of sorafenib and antimiRNA21 for enhanced hepatocellular carcinoma therapy. *Acta Biomater*. 2018;75:413–426. doi:10.1016/j.actbio.2018.05.049
13. Luo X, Li A, Chi X, et al. Hypoxia-activated prodrug enabling synchronous chemotherapy and HIF-1α downregulation for tumor treatment. *Bioconjug Chem*. 2021;32(5):983–990. doi:10.1021/acs.bioconjchem.1c00131
14. Shin DH, Kim JH, Jung YJ, et al. Preclinical evaluation of YC-1, a HIF inhibitor, for the prevention of tumor spreading. *Cancer Lett*. 2007;255(1):107–116. doi:10.1016/j.canlet.2007.03.026
15. Shi L, Shen W, Davis MI, et al. SULT1A1-dependent sulfonation of alkylators is a lineage-dependent vulnerability of liver cancers. *Nat Cancer*. 2023;4(3):365–381. doi:10.1038/s43018-023-00523-0
16. Liao W, Calvisi DF, Chen X. A new mission for an old anti-cancer drug: harnessing hepatocyte-specific metabolic pathways against liver tumors. *Signal Transduct Target Ther*. 2023;8(1):240. doi:10.1038/s41392-023-01513-5
17. Ouyang C, Zhang J, Lei X, et al. Advances in antitumor research of HIF-1α inhibitor YC-1 and its derivatives. *Bioorg Chem*. 2023;133:106400. doi:10.1016/j.bioorg.2023.106400
18. Li Y, Zhang MZ, Zhang SJ, et al. HIF-1α inhibitor YC-1 suppresses triple-negative breast cancer growth and angiogenesis by targeting PlGF/VEGFR1-induced macrophage polarization. *Biomed Pharmacother*. 2023;161:114423. doi:10.1016/j.biopha.2023.114423
19. Wang SW, Pan SL, Guh JH, et al. YC-1 [3-(5'-Hydroxymethyl-2'-furyl)-1-benzyl Indazole] exhibits a novel antiproliferative effect and arrests the cell cycle in G0-G1 in human hepatocellular carcinoma cells. *J Pharmacol Exp Ther*. 2005;312(3):917–925. doi:10.1124/jpet.104.077230
20. Wang M, Zhai Y, Ye H, et al. High co-loading capacity and stimuli-responsive release based on cascade reaction of self-destructive polymer for improved chemo-photodynamic therapy. *ACS Nano*. 2019;13(6):7010–7023. doi:10.1021/acsnano.9b02096
21. Xiong F, Qin Z, Chen H, et al. pH-responsive and hyaluronic acid-functionalized metal-organic frameworks for therapy of osteoarthritis. *J Nanobiotechnology*. 2020;18(1):139. doi:10.1186/s12951-020-00694-3
22. Wu Y, Zhu R, Zhou M, et al. Homologous cancer cell membrane-camouflaged nanoparticles target drug delivery and enhance the chemotherapy efficacy of hepatocellular carcinoma. *Cancer Lett*. 2023;558:216106. doi:10.1016/j.canlet.2023.216106
23. Zhou T, Liang X, Wang P, et al. A hepatocellular carcinoma targeting nanostrategy with hypoxia-ameliorating and photothermal abilities that, combined with immunotherapy, inhibits metastasis and recurrence. *ACS Nano*. 2020;14(10):12679–12696. doi:10.1021/acsnano.0c01453
24. Gao Y, Zheng QC, Xu S, et al. Theranostic nanodots with aggregation-induced emission characteristic for targeted and image-guided photodynamic therapy of hepatocellular carcinoma. *Theranostics*. 2019;9(5):1264–1279. doi:10.7150/thno.29101
25. Yang G, Xu L, Chao Y, et al. Hollow MnO(2) as a tumor-microenvironment-responsive biodegradable nano-platform for combination therapy favoring antitumor immune responses. *Nat Commun*. 2017;8(1):902. doi:10.1038/s41467-017-01050-0
26. Fornaguera C, Dols-Perez A, Calderó G, García-Celma MJ, Camarasa J, Solans C. PLGA nanoparticles prepared by nano-emulsion templating using low-energy methods as efficient nanocarriers for drug delivery across the blood-brain barrier. *J Control Release*. 2015;211:134–143. doi:10.1016/j.jconrel.2015.06.002
27. D'Souza AA, Shegokar R. Polyethylene glycol (PEG): a versatile polymer for pharmaceutical applications. *Expert Opin Drug Deliv*. 2016;13(9):1257–1275. doi:10.1080/17425247.2016.1182485
28. Zhao J, Mi Y, Liu Y, Feng SS. Quantitative control of targeting effect of anticancer drugs formulated by ligand-conjugated nanoparticles of biodegradable copolymer blend. *Biomaterials*. 2012;33(6):1948–1958. doi:10.1016/j.biomaterials.2011.11.051
29. Zhou F, Feng B, Wang T, et al. Theranostic prodrug vesicles for reactive oxygen species-triggered ultrafast drug release and local-regional therapy of metastatic triple-negative breast cancer. *Adv Funct Mater*. 2017;27(46):1703674. doi:10.1002/adfm.201703674
30. Zhen S, Wang S, Li S, et al. Efficient Red/Near-Infrared Fluorophores Based on Benzo[1,2-b:4,5-b′]dithiophene 1,1,5,5-Tetraoxide for targeted photodynamic therapy and in vivo two-photon fluorescence bioimaging. *Adv Funct Mater*. 2018;28(13):1706945. doi:10.1002/adfm.201706945
31. Yu KH, Hung HY. Synthetic strategy and structure-activity relationship (SAR) studies of 3-(5'-hydroxymethyl-2'-furyl)-1-benzyl indazole (YC-1, Lificiguat): a review. *RSC Adv*. 2021;12(1):251–264. doi:10.1039/d1ra08120a
32. Granito A, Forgione A, Marinelli S, et al. Experience with regorafenib in the treatment of hepatocellular carcinoma. *Therap Adv Gastroenterol*. 2021;14:17562848211016959. doi:10.1177/17562848211016959
33. Modarres-Gheisari SMM, Gavagsaz-Ghoachani R, Malaki M, Safarpour P, Zandi M. Ultrasonic nano-emulsification - A review. *Ultrason Sonochem*. 2019;52:88–105. doi:10.1016/j.ultsonch.2018.11.005
34. Wang C, Wang M, Wang Y, et al. Construction and characterization of novel hydrophilic nanospheres loaded with lambda-cyhalothrin via ultrasonic emulsification-solvent evaporation. *Int J Mol Sci*. 2022;23(22). doi:10.3390/ijms232214063
35. Lopes MA, Abrahim-Vieira B, Oliveira C, et al. Probing insulin bioactivity in oral nanoparticles produced by ultrasonication-assisted emulsification/internal gelation. *Int J Nanomed*. 2015;10:5865–5880. doi:10.2147/ijn.S86313

36. Wu L, Qiao L, Zhang S, et al. Dual-engineered macrophage-microbe encapsulation for metastasis immunotherapy. *Adv Mater*. 2024;36(36): e2406140. doi:10.1002/adma.202406140
37. Hao Y, Chen Y, He X, et al. RGD peptide modified platinum nanozyme Co-loaded glutathione-responsive prodrug nanoparticles for enhanced chemo-photodynamic bladder cancer therapy. *Biomaterials*. 2023;293:121975. doi:10.1016/j.biomaterials.2022.121975
38. Dudas B, Toth D, Perahia D, Nicot AB, Balog E, Miteva MA. Insights into the substrate binding mechanism of SULT1A1 through molecular dynamics with excited normal modes simulations. *Sci Rep*. 2021;11(1):13129. doi:10.1038/s41598-021-92480-w
39. Hempel N, Gamage N, Martin JL, McManus ME. Human cytosolic sulfotransferase SULT1A1. *Int J Biochem Cell Biol*. 2007;39(4):685–689. doi:10.1016/j.biocel.2006.10.002